ARTICLE

Check for updates

Injection spectroscopy of momentum state lattices

Sai Naga Manoj Paladugu [1,3], Tao Chen [1,2,3], Fangzhao Alex An[1,3], Bo Yan[2] & Bryce Gadway [1✉]

The energy spectrum of quantum systems contain a wealth of information about their underlying properties. Spectroscopic techniques, especially those with access to spatially resolved measurements, can be challenging to implement in real-space systems of cold atoms in optical lattices. Here we explore a technique for probing energy spectra in synthetic lattices that is analogous to scanning tunneling microscopy. Using one-dimensional synthetic lattices of coupled atomic momentum states, we explore this spectroscopic technique and observe qualitative agreement between the measured and simulated energy spectra for small two- and three-site lattices as well as a uniform many-site lattice. Finally, through simulations, we show that this technique should allow for the exploration of the topological bands and the fractal energy spectrum of the Hofstadter model as realized in synthetic lattices.

[1] Department of Physics, University of Illinois Urbana-Champaign, Urbana, IL 61801-3080, USA. [2] Interdisciplinary Center of Quantum Information, State Key Laboratory of Modern Optical Instrumentation, and Zhejiang Province Key Laboratory of Quantum Technology and Device and Department of Physics, Zhejiang University, Hangzhou 310027, China. [3]These authors contributed equally: Sai Naga Manoj Paladugu, Tao Chen, Fangzhao Alex An.
✉email: bgadway@illinois.edu

Cold atom systems are well suited to Hamiltonian engineering for the exploration of condensed matter physics phenomena. To help explore these systems, a suite of techniques have been developed over the past decades to reveal the energy spectra in cold atom experiments, including injection spectroscopy based on auxiliary spin components[1–3], lattice amplitude modulation spectroscopy[4,5], phasonic modulation spectroscopy in quasiperiodic lattices[6], momentum-resolved band spectroscopy[7,8], and Fourier transform spectroscopy[9]. On their own, such probes are primarily global and do not provide a direct window into the local spatial structure of states that comprise the spectrum of a system.

Local spectroscopy would be of particular interest for certain problems related to disordered[10] or topological[11] systems. For example, in topological systems, local spectroscopic probing at the boundary or within the bulk could reveal distinct responses and serve to indicate the presence of topological boundary modes. In disordered or quasiperiodic systems, the probing of mobility edges[12–15] could be better facilitated by local probes that distinguish between metallic and insulating states in a energy-resolved manner.

We demonstrate such a local spectroscopic probe that is suitable for synthetic lattice of coupled momentum states. Similar spin-injection spectroscopy techniques have been used to explore spin–orbit coupling in atomic Fermi gases[1–3]. Indeed, it is natural to consider the extension of such techniques to synthetic lattices[16] that consist of discrete states[17–20], and in particular, discrete momentum states in ultracold[21–23] and room-temperature gases[24–29]. By considering part of a synthetic lattice as a "probe" attached to a "system" of interest, and using the suite of controls afforded in synthetic lattice experiments, we study the energy-dependence of probe-system coupling to directly determine the energy spectrum of dressed states in a synthetic lattice system. This builds upon previous explorations using coupled momentum states that used system–reservoir coupling to

engineer effective non-Hermitian loss[22,30], as well as related demonstrations of energy-resolved spectroscopy in topological synthetic lattices of microwave-coupled Rydberg levels[31] and non-Hermitian momentum state lattices[32]. Our technique is also similar to ones that have been proposed theoretically, such as the use of microscopy to observe the internal state dynamics of atoms trapped in a cavity[33], as well as the probing of quantum many-body states in optical lattices by energy-resolved atom injection[34] and removal[35]. We demonstrate this technique on the simple test cases of few-site and many-site tight-binding lattices, finding qualitative agreement with theoretical predictions as well as observing the influence of atomic interactions. Using numerical simulations, we demonstrate the applicability of this technique for studies of topological band structures, including the celebrated Hofstadter butterfly spectrum and its associated topological boundary states.

Results and discussion

Theory. We begin by considering the following Hamiltonian that describes the injection site, the discrete lattice under study, and their coupling:

$$\hat{H} = \hat{H}_{\text{inj}} + \hat{H}_{\text{latt}} \tag{1}$$

$$\hat{H}_{\text{inj}} = t_{\text{inj}}|0\rangle\langle 1| + t_{\text{inj}}|1\rangle\langle 0| + E_{\text{inj}}|0\rangle\langle 0| \tag{2}$$

$$\hat{H}_{\text{latt}} = \sum_{j=1}^{N-1}\left(t_j|j+1\rangle\langle j| + \text{h.c.}\right) + \sum_{j=1}^{N} E_j|j\rangle\langle j|. \tag{3}$$

Here, $|0\rangle$ represents the probe site, $|1\rangle$ represents the injection site (which is part of the lattice, $\hat{H}_{\text{latt}}$), t_{inj} is the injection tunneling between the probe site and the lattice, E_{inj} is the energy detuning of the probe site with respect to the lattice, N is the number of lattice sites, and the t_j are the (in general link-specific) tunneling terms within the lattice itself (depicted in Fig. 1a). We restrict t_{inj} to be real-valued, while the t_j can be complex. Let the ϵ_i

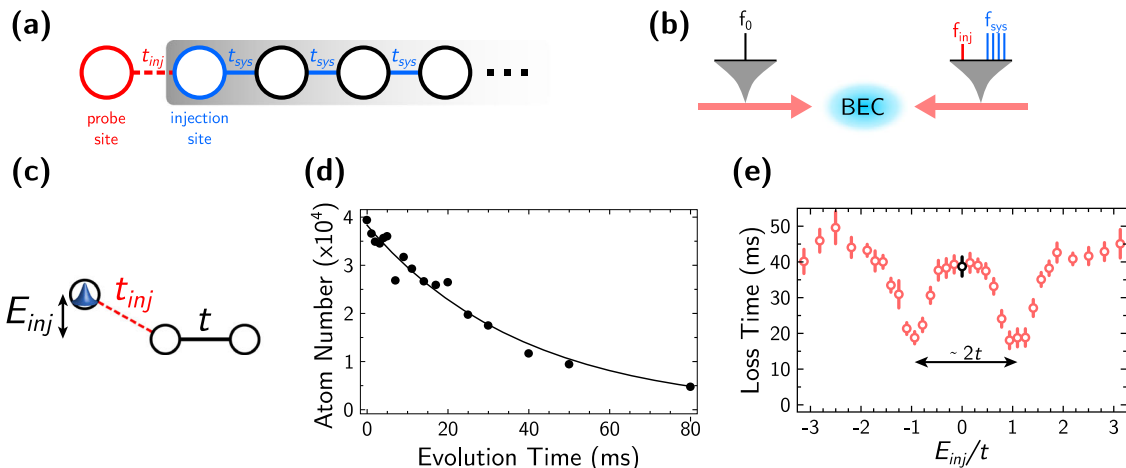**Fig. 1 Energy-resolved injection spectroscopy in synthetic momentum state lattices. a** To probe a lattice system having characteristic tunneling energy t_{sys}, population is weakly injected in from a nearby probe site through a probe-system coupling term t_{inj}. **b** In synthetic lattices of atomic momentum states, the system, probe, and all relevant coupling terms can be engineered through the spectral addressing of unique Bragg resonances. Here, two counter-propagating beams interfere to drive Bragg transitions between adjacent states with momenta $2n\hbar k$ and $2(n+1)\hbar k$, where $k = 2\pi/\lambda$ and λ is the wavelength of the driving laser fields (1064 nm in experiment). **c** Illustration of the simplest two-site lattice system with inter-site hopping term $t = h \times 1598(10)$ Hz, along with a control of the energy bias E_{inj} of the probe site relative to zero energy [$t_{\text{inj}} = h \times 40(10)$ Hz]. In practice, this bias tuning is accomplished simply through a change in the frequency of the applied injection tone, i.e., the spectral component labeled f_{inj} in (**b**). In the weak-coupling limit ($t_{\text{inj}} \ll t_{\text{sys}}$), the rate of population loss from the probe into the system provides a measure of the local density of system states at the injection site. **d** For injection into the two-site system at zero bias, we show the dynamics of the measured atomic population in the probe site, along with an exponential fit used to extract a characteristic loss time. **e** Measured loss time plotted vs. the injection site energy bias. The black data point at $E_{\text{inj}}/t = 0$ relates to the loss time extracted from (**d**). The two peaks of enhanced loss rates, centered around $E_{\text{inj}} = \pm t$, correspond to the symmetric and anti-symmetric eigenstates of the double well system. The error bars in **e** relate to the standard error of the fit-determined $1/e$ loss times.

be the eigenvalues and $|\psi_i\rangle$ be the eigenvectors for the lattice Hamiltonian, Eq. (3). In general, we can write

$$|\psi_i\rangle = \sum_{n=1}^{N} c_n^{(i)} |n\rangle. \quad (4)$$

If $t_{\text{inj}} \ll t_j$, then we can treat the injection Hamiltonian as a perturbation. In this limit, we can use Fermi's golden rule in order to characterize the loss rate from the probe site into the lattice:

$$\Gamma = \frac{2\pi}{\hbar} \sum_{i=1}^{N} |\langle \psi_i | \hat{H}_{\text{inj}} | 0 \rangle|^2 \delta(E_i - E_{\text{inj}}) \quad (5)$$

$$= \frac{2\pi}{\hbar} t_{\text{inj}}^2 \sum_{i=1}^{N} |c_1^{(i)}|^2 \delta(E_i - E_{\text{inj}}). \quad (6)$$

In a real experiment, the delta function will become regularized due to the finite amount of evolution time, resulting in a Fourier-limited energy resolution. Still, for sufficiently long evolution times and sufficiently small values of t_{inj}, a measurement of the loss rate as a function of E_{inj} will permit an energy-resolved measurement of the local density of states. Roughly speaking, the loss rate from the probe site will be enhanced if E_{inj} is set close to the energy of a lattice eigenstates and will vanish if there are no lattice eigenstates in the vicinity of E_{inj}.

One useful feature of injection spectroscopy is its sensitivity to the details of the eigenstate weight at the site of injection (i.e., its local nature). At the resonance condition ($E_{\text{inj}} = E_i$) for some eigenstate $|\psi_i\rangle$, the rate of loss from the probe site will be proportional to the overlap, or Franck–Condon factor, $|\langle 1 | \psi_i \rangle|^2$. The more weight the eigenstate has with the site of injection, the larger the loss rate. This sensitivity to the *local* density of states should prove useful when, for example, probing the distinction between the bulk and edge spectra of a topological system[17,18,36]. In disordered or pseudo-disordered systems, this feature can also be useful for detecting metal–insulator transitions and for identifying mobility edges[14,37].

Two- and three-site lattices. The simplest system we perform spectroscopy on is a two-site lattice with tunneling strength $t = h \times 1598(10)$ Hz and injection tunneling strength $t_{\text{inj}} = h \times 40(10)$ Hz. The eigenenergies for this lattice are simply $E = \pm t$, and the eigenstates are equal symmetric and anti-symmetric superpositions of atoms at the left and right site. When we perform spectroscopy on the two-site lattice, we see that away from $E_{\text{inj}}/t = \pm 1$ the experimental loss time is approximately 40 ms. We observe two features of decreased loss times in Fig. 2), relating to dips in the data near the expected resonances at $E_{\text{inj}}/t = \pm 1$.

This observation can also be understood as Autler–Townes splitting of the bare probe-injection site transition due to hybridization of the states $p = 2\hbar k$ and $4\hbar k$ by the applied Bragg field.

The next simplest system is the three-site lattice with uniform tunneling strength $t = h \times 2040(3)$ Hz and injection tunneling strength $t_{\text{inj}} = h \times 50(3)$ Hz. The energies for this type of lattice are $E = 0, \pm\sqrt{2}t$. When we perform spectroscopy on the three-site lattice, we see a similar trend as before, shown in Fig. 2b. When E_{inj} is nearly resonant with an eigenenergy of the lattice, the loss time decreases. When E_{inj} is away from the eigenenergies of the lattice, the loss time is roughly constant. One feature of the three-site loss spectrum is that the loss time dips appear to be shifted downward in energy relative to their naive expectation values. Indeed, as seen also in the numerically simulated curve, one should expect a slight downward shift in energy due to the ac Stark shifts of the momentum states, i.e., due to the fact that the strong tunneling links in the lattice induce momentum-dependent light shifts that shift the lattice site energies relative to the probe site.

For these two simplest cases, we note that the predicted loss curves generated from the GPE simulations match the locations of the dips in the spectrum but do not perfectly match the scale of the experimentally measured loss time. For the two-site case, the loss time away from the eigenergies is measured to be approximately 40 ms, while the simulation predicts the loss time should be closer to 90 ms. It is again interesting to note that, as seen more clearly in the simulated spectrum, there is a slight downward shift in energy due to the large system tunneling, which results in momentum-dependent ac Stark shift to the synthetic lattice site energies.

For the three-site lattice, the loss time away from the eigenergies is measured to be approximately 15 ms, while the simulation predicts it should be roughly 80 ms. While the GPE simulation does account for the fact that the cloud separates spatially, thus limiting the coherence of the time evolution, it does not account for additional loss mechanisms. Two possible mechanisms could include momentum-changing s-wave collisions between momentum orders, which scatter atoms into modes outside of those considered, as well as scattering between thermal and condensed atoms. Furthermore, there are oscillations in the simulated spectra which are not captured in the experimental data, which is likely due to the fact that there are additional loss mechanisms and inhomogeneous density shifts that wash them out.

We note that the simulations also account for the effects of mode-preserving atomic interactions (effectively local attractive nonlinearities)[38], which effectively serve to shift the energy of the
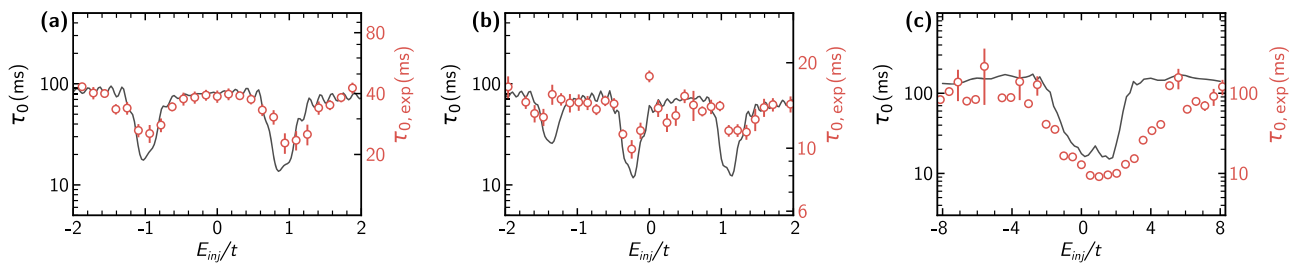

Fig. 2 Experimental and theoretical loss times for three different lattices. The simulated curves are in black and the experimental data are in red. **a** The loss times for spectroscopy of a two-site lattice as a function of E_{inj} (in units of the lattice hopping energy t). This panel of data is the same as in Fig. 1a, with $t = h \times 1598(10)$ Hz and $t_{\text{inj}} = h \times 40(10)$ Hz. Note that the vertical axes for the simulation and the experimental data are on different scales. **b** The loss times for injection into a three-site lattice with uniform system hopping $t = h \times 2040(3)$ Hz and $t_{\text{inj}} = h \times 50(3)$ Hz. We again note the different vertical axes for the simulation and experimental data. **c** The loss time as measured by injection spectroscopy of a uniform 26-site lattice. Here, we operate with a uniform system hopping $t = h \times 492(10)$ Hz and with $t_{\text{inj}} = h \times 50(10)$ Hz, and the simulations and data have common vertical axes. The error bars in **a** and **b** reflect the standard error of the fit $1/e$ loss time. The error bars in (**c**) relate to the standard error of the measured probe population, propagated to an error in the $1/e$ time constant.
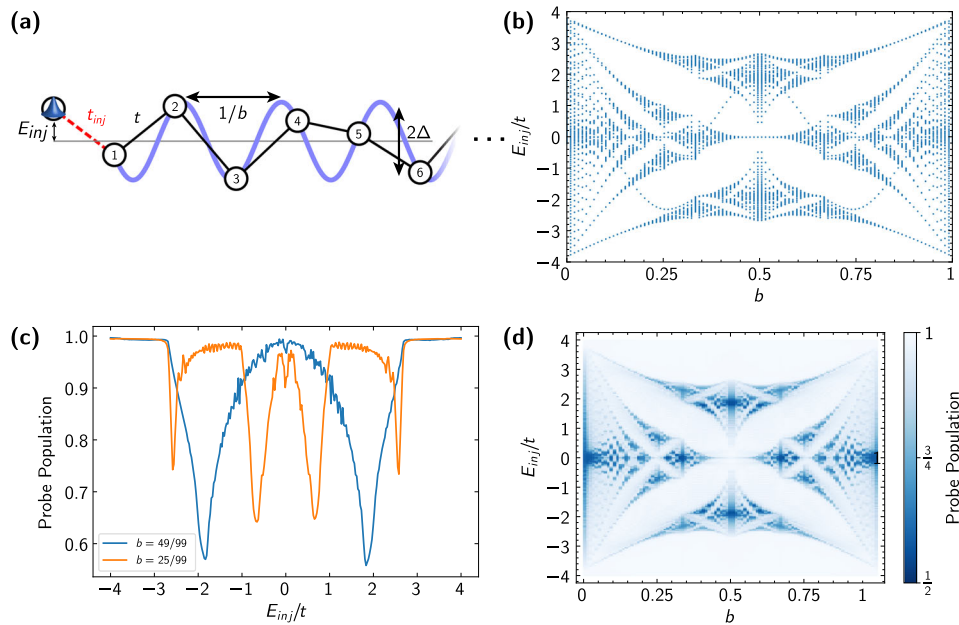
Fig. 3 Injection spectroscopy of an Aubry–André–Harper–Hofstadter (AAHH) lattice. a A qualitative depiction of the AAHH lattice under injection spectroscopy. At the left end, a probe site has an adjustable site energy E_{inj} and is coupled into the lattice with a tunneling rate t_{inj}. In the AAHH lattice, the sites are uniformly coupled with nearest-neighbor tunneling rates t, but site-dependent energies ε_i are quasiperiodically shifted as $\Delta \cos(2\pi bi + \phi)$. Here, Δ is the modulation depth, b is the incommensurability parameter, and ϕ is the phason value. **b** The calculated energy spectrum for the open AAHH chain for $\phi = 0$ and $\Delta/t = 9/5$, with $t = 1$, taken for different values of the incommensurability parameter b. **c** Two numerical simulations of the injection loss spectrum, relating to the fractional population remaining at the probe site as a function of the injection site energy, for incommensurability parameters $b = 49/99$ and $b = 25/99$ (both for $\Delta/t = 9/5$ and $t_{inj}/t = 1/20$). These spectra are ϕ-averaged over 100 uniformly spaced values of $\phi \in [-\pi, \pi]$. The probe population is calculated after 150 system tunneling times. **d** A composite plot of ϕ-averaged injection spectra as in (**c**), but for a larger range of incommensurability parameter values $b \in [0, 1]$.

lattice system up relative to the populated probe site. In the two-site case, this upwards shift (relative to the probe) due to interactions and the downwards shift due to the ac Stark effect are nearly perfectly compensated. However, in the three-site case, where we operate with a larger tunneling amplitude, the downwards shift due to the ac Stark effect dominates.

Uniform lattice. The last system we probe experimentally is a uniform chain with tunneling strength $t = h \times 492(10)$ Hz with the injection link strength $t_{inj} = h \times 50(10)$ Hz. Such a lattice has eigenenergies ranging from $-2t$ to $2t$. For this spectrum, instead of measuring the loss rate by taking measurements at a range of evolution times, we rather directly measured the amount of population remaining in the $p = 0$ order after an evolution time of 20 ms. We then extract the loss time by solving $P(20\,\mathrm{ms}) = P(0)e^{-(20\mathrm{ms})/\tau_0}$ for τ_0, assuming a fixed initial population of $P(0) = 6 \times 10^4$ atoms. We see that there is a broad dip in the loss time for a range of E_{inj} values near zero energy, with a positive shift that is qualitatively captured by the simulated curve shown in Fig. 2c. This positive shift is due to the fact that the population in the $p = 0$ order is larger than the population in any of the other lattice sites, which induces a mean field shift in the site energy of the $p = 0$ order down by $U \approx 1.5t$. This has the relative effect of shifting the entire unoccupied spectrum up in energy by U. Note that the interaction shift effect is less pronounced in the two- and three-site lattices because those experiments were undertaken with a larger value of the system tunneling t. In the uniform lattice, the effect of the light shift is also much smaller than in our previous two- and three-site lattice cases because the tunneling strength is roughly a third what we used in the two-site lattice and a fourth of what we used in the three-site lattice. The simulated curve is not as broad as the experimental data, however. This may

likely be due to the fact that the BEC in the experiment has an inhomogeneous density, which gives rise to density-dependent mean-field interaction shifts and broadening of the response lineshape.

Limitations and further improvements. From the three experiments discussed above, we posit that there are two main technical limitations that can be addressed to improve the resolution of the technique: limits on the timescale of allowable coherent evolution and broadening of the spectral response that results from the inhomogeneous atomic density and the density-dependent (Hartree-like) spectral shifts to the Bragg transitions. In contrast, the method proposed in[35] is limited by averaging of the atomic current from the system to probe over a finite time interval, in addition to the finite bandwidth of the probe lattice. In our scheme, the probe has no such structure, and in principle, the spectral resolution should be limited by the bandwidth or strength of the injection link.

Considering just single-particle effects, a kind of "Welcher-Weg" decoherence results from the loss of spatial overlap between the probe and the momentum states (and dress states) of the system under interrogation. This technical issue can be mitigated by working with more spatially extended atomic samples, such as in a large box trap or by using low harmonic trapping frequencies.

For the present experiments, the major limitation appears to result from the inhomogeneous density-dependent spectral shifts. One could utilize flat-bottom or box traps[39,40] to achieve a more uniform atomic density. This would still enable the exploration of how interactions modify the spectral response. Alternatively, if one is seeking the best possible energy resolution to identify some subtle features, such as the fractal energy structure of the
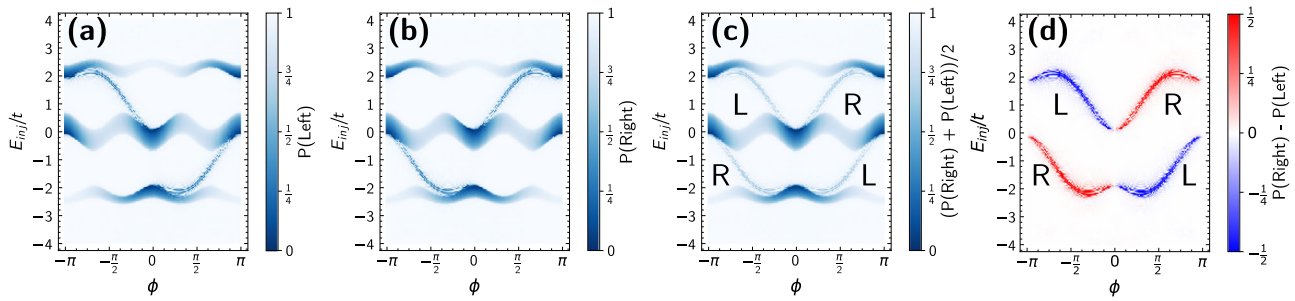
Fig. 4 Boundary-dependent injection into the Aubry–André–Harper–Hofstadter (AAHH) lattice. Energy- and phason-resolved injection spectroscopy of a 101-site AAHH lattice lattice for $\Delta/t = 9/5$, an incommensurability ratio $b = 1/3$, and $t_{inj}/t = 1/20$. **a** For probing from the left boundary, fractional population remaining at the probe site (indicated by the color scale at right) as a function of the probe site energy E_{inj} and the phason value ϕ after a total of 150 system tunneling times. Three bulk energy bands are observed, as well as prominent dispersing inter-band modes. **b** Same measure as in (**a**), but for the case of probing from the right boundary. **c** The average of the injection spectroscopy signal for the left- and right-sided injection. **d** The difference between the left- and right-sided injection signals, revealing on the presence of the topological boundary states on the right (in red) and left (in blue) system boundaries.

Hofstadter butterfly, one could instead simply take advantage of a suitable Feshbach resonance in an atom such as ^{39}K and tune the s-wave scattering length[41–43] to near zero. This approach would additionally mitigate other effects like inelastic scattering to momentum modes outside of the "momentum lattice" state space.

Aubry–André–Harper–Hofstadter model. The Harper–Hofstadter (HH) model is used to describe the motion of an electron in a lattice that is placed in a uniform external magnetic field. In cold atoms, the two-dimensional HH model been realized for cold atoms using techniques of laser-assisted hopping in real-space lattices[44,45]. The two- and three-dimensional versions of the HH model can also be effectively reduced to the problem of a one-dimensional periodically modulated lattice model, where the periodicity of the modulation is set by the ratio Φ/Φ_0, with Φ the amount of magnetic flux through a plaquette and $\Phi_0 = h/e$ is the quantum of flux[46,47]. This dimensionally-reduced model, the Aubry–André–Harper–Hofstadter (AAHH) model, has played an important role in explorations of localization phenomena with cold atoms[13,14,48,49] and for studies of topological edge states[50–53].

One longstanding goal of studies of the HH model is to directly measure its fractal energy spectrum, namely the famous "Hofstadter butterfly." While there are proposals to observe the butterfly spectrum in driven optical lattices[6], there has not yet been a method proposed to observe it in a synthetic lattice. Here, we show that the injection spectroscopy technique may prove useful for the measurement of the HH butterfly spectrum, and for the measurement of the corresponding topological edge states.

To be concrete, the model we consider is given by the AAHH tight-binding Hamiltonian:

$$\hat{H} = -\sum_{i=1}^{N-1} t(|i\rangle\langle i+1| + \text{h.c.}) + \sum_{i=1}^{N} \Delta \cos(2\pi b i + \phi)|i\rangle\langle i|. \quad (7)$$

Here, t is the tunneling strength between nearest neighbors, Δ is the strength of the potential energy modulation, $1/b$ is the periodicity of the site-energy modulation, and ϕ is the phason degree of freedom, relating to a phase shift to the sinusoidal potential modulation. Note that for rational values of b the site potential modulation is periodic, but for irrational b the site potential energy shifts will never repeat. This model is shown schematically in Fig. 3a, along with its fractal energy eigenstate spectrum as a function of the incommensurability parameter b, shown in Fig. 3b.

In our theoretical study, we first consider the AAHH model with $\Delta/t = 9/5$ for various b. The number of sites is $N = 101$. We begin by having all the population start in the site $|p = 0\hbar k\rangle$, and

we let the system evolve for 150 tunneling times. At the end of each simulation, we record the population that is left in the $|p = 0\hbar k\rangle$ site. We repeat this calculation for many different energy offset values of the probe site to get the spectrum for one value of b. Two such loss spectra, for values of $b = 24/99(\sim 1/4)$ and $b = 49/99(\sim 1/2)$, are shown in Fig. 3c. These spectra reveal four and two primary loss features, respectively, relating to the existence of a corresponding number of bulk mini-bands for these values of the incommensurability parameter b. We can repeat this simulation for a large range of b values, keeping Δ/t constant, and we find the emergence of the famous Hofstadter butterfly spectrum shown in Fig. 3d. These simulations of tunneling-based loss spectra match qualitatively with the full numerically calculated spectrum shown in Fig. 3b. Note that some eigenvalues are not represented well in our simulated spectrum, likely due to the fact that they correspond to eigenvectors that have very little (or no) weight at the site of injection ($|1\rangle$). We note that these simulations assume a large timescale of relevant tunneling times, however these structures may still be resolved for shorter probing times, especially in the somewhat trivial strong Δ limit (if averaging over the phason degree of freedom).

In Fig. 4, we show how one may probe the topological edge states associated with the AAHH spectrum. We fix b to 1/3 and Δ/t to 9/5 and we vary the value of ϕ, which is related to the k_y wave vector of the higher-dimensional HH model. We perform two sets of simulations corresponding to injection at opposite sides of the open-boundary AAHH lattice. In one set of simulations, we start in the $|p = 0\rangle$ state and construct the lattice with sites $|p = 2n\hbar k\rangle$, where $n \geq 1$. We call this the "left injection" configuration. For a fixed ϕ, we repeat this simulation for many different E_{inj} values in order to produce a loss spectrum. In the alternate set of simulations, we begin in the $|p = 0\rangle$ state and we construct the lattice with sites $|p = 2n\hbar k\rangle$, where $n \leq -1$; we call this the "right injection" configuration. The left and right injection spectra are shown in Fig. 4a and Fig. 4b, respectively. In both spectra, there are three bands, as well as two modes that disperse between the bulk bands. The combination (average) of the two spectra reveals the entire spectrum, including bulk and boundary states, as is shown in Fig. 4c. We can also take the difference between the left and right injection spectra; this subtraction (shown in Fig. 4d) effectively removes the bulk bands, revealing the topological edge modes as well as the edge they live on.

Scanning mode spectroscopy. Here, we describe an extension of the one-dimensional techniques in order to probe the bulk as well
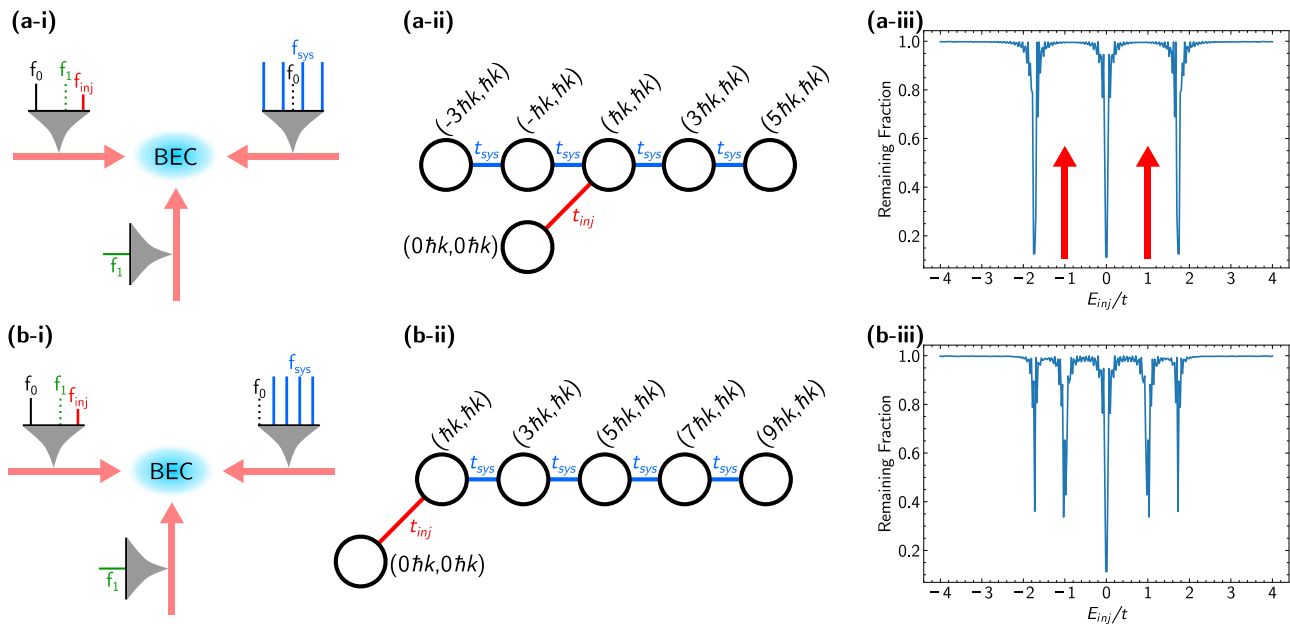
Fig. 5 "Scanning mode" spectroscopy of momentum state lattices. a-i Here, we show the layout for generating a quasi two-dimensional lattice. There are two counter-propagating laser beams that generate the lattice, and one beam orthogonal to both counter-propagating beams. The orthogonal beam provides the link between the injection site and the lattice. **a-ii** The three beams in (**a-i**) couple different momentum sites as shown here. The transition frequencies in the counter-propagating beam are chosen such that the probe site is connected to a site in the middle of the lattice. **a-iii** A simulated loss spectrum for the situation depicted in (**a-ii**), where initially all of the population is in the injection site. Here, $t_{inj}/t_{sys} = 1/20$ and we plot the remaining fraction of the population in the probe after 150 tunneling times. **b-i** Here we depict the frequencies necessary to make a lattice where the probe site is attached to the left edge of a uniform five-site lattice. **b-ii** The lattice beams interfere to make the effective five-site tight binding lattice with uniform tunneling, plus a probe site attached to the left edge of the lattice. **b-iii** Simulated spectrum for the situation depicted in (**b-ii**). Again, all of the population initially starts in the probe site, and fixing $t_{inj}/t_{sys} = 1/20$ we plot the remaining probe fraction after 150 tunneling times. Notice that there are two additional dips that were not present if we only probed into the center of the lattice.

as edge states. As we stated in previous sections, it is possible to miss certain eigenenergies if the corresponding eigenvector has no weight in the site to which the probe site is connected to. In particular, it is possible to miss states which have their wave function mostly or entirely in the bulk of the one-dimensional lattice. In order to counteract this, it would be useful to have a scheme where we can attach the probe site to any site in the lattice.

In order to probe any site in the lattice, in more direct analogy to scanning probe techniques[54], we can extend the considered one-dimensional momentum- state lattice to a quasi two-dimensional geometry. In practice, this could be enabled by adding an additional laser beam that propagates in the direction perpendicular to the original two counter-propagating beams, as is shown in Fig. 5a-i. Interference between the frequency component f_1 on the up-traveling beam and the frequency component f_{inj} on the right-traveling beam can drive Bragg transitions from the $|0\hbar k, 0\hbar k\rangle$ state to the $|\hbar k, \hbar k\rangle$ state. We can then construct the frequency tones, f_{sys} on the left-traveling beam such that their interference with the frequency tone f_0 on the right-traveling beam resonantly drives transitions between the momentum states $|\hbar k, (2n + 1)\hbar k\rangle$ and $|\hbar k, (2n + 3)\hbar k\rangle$, where n is an integer, in order to construct a one-dimensional lattice of initially unoccupied states, as depicted in Fig. 5a-ii. In order to prevent unwanted interference effects, the frequency difference between f_0 and f_1 are set to be many orders of magnitude above, say, the recoil energy $E_R = \hbar^2 k^2 / 2M$, while the frequency difference between (f_0, f_{sys}) and (f_1, f_{inj}) are, respectively, on the order of the recoil energy. As one simple example, we consider probing a uniform one dimensional lattice with some tunneling strength t_{sys}, by injecting into the center site as shown in Fig. 5a-ii. When the energy of the probe is scanned, it reveals

three loss features, as seen in the simulated spectrum shown of Fig. 5a-iii. In this case, two eigenstates of the system under consideration (the five-site uniform lattice) are not revealed by the loss measurement due to symmetry—they have exactly zero weight at the site of injection.

In this "scanning mode" injection spectroscopy, the frequency spectrum of the left-traveling beam can be altered to that depicted in Fig. 5b-i, such that the injection site ($|\hbar k, \hbar k\rangle$) actually resides at the left end of the five-site lattice, as shown in Fig. 5b-ii. The corresponding loss spectrum in Fig. 5b-iii for this configuration reveals five loss features, corresponding to the full set of eigenstates of this system, including the two modes at energies of $\pm t$ that were missed by the center-site injection.

This simple example shows how tunneling spectroscopy in synthetic lattices may be further extended to a "scanning mode" to allow for greater utility in characterizing different model systems. Beyond this, injection spectroscopy in synthetic lattice systems can even be extended to include simultaneous injection at multiple sites of a system (with control of the relative amplitude and phase of injection at different locations). This very unique capability can, for example, be used to perform (approximations to) wavevector-resolved spectroscopy as well as band-specific spectroscopy in multi-band systems with multi-site unit cells, and has been theoretically investigated for a two-dimensional Lieb lattice of synthetically-coupled momentum states[55].

Conclusion

Synthetic lattices in cold atom systems offer a powerful window into the physics of many condensed matter phenomenon such as localization, topological insulators, and the quantum Hall effect. In this work, we have shown how it is possible to probe the spectrum of one-dimensional synthetic lattices made by laser-

coupled momentum states. Experimentally, for the examples of two-site, three-site, and many-site uniform lattices, we have shown that it is possible to reproduce the eigenenergy locations through observed loss resonances from an injected probe site. By comparing to numerical (GPE model) simulations, we found that the experimental data exhibited qualitative agreement with the expected locations of resonant loss features in these systems, including mean-field shifts due to atomic interactions. Additionally, through numerical simulations, we have shown theoretically that this injection spectroscopy technique could allow for energy spectrum studies of the AAHH model, opening the way to the measurement of fractal energy spectra and topological boundary states in synthetic lattices.

Methods

In our experiment, we typically start with nearly pure Bose–Einstein condensates (BEC) of roughly 5×10^{4} ^{87}Rb atoms confined in a crossed-dipole trap formed from lasers of wavelengths 1064 nm and 1070 nm. These trapping beams create a harmonic trap with trap frequencies $\omega_{x,y,z} \approx 2\pi \times \{130, 10, 130\}$ Hz. After forming the BEC, we suddenly turn on a retro-reflected path of the 1064 nm beam that contains a tailored frequency spectrum of discrete components. The resulting interference of the two counter-propagating beams having wavelength $\lambda = 1064$ nm serves to couple discrete atomic momentum orders $p_n = 2n\hbar k$ (with $k = 2\pi/\lambda$) via two-photon Bragg transitions. As summarized in Fig. 1b, the Bragg transitions serve to form a synthetic lattice of momentum states[56,57], as well as introduce an injection link between a probe site and the lattices under study.

More explicitly, the initially populated $p = 0$ momentum order serves as the "probe site," and resides next to the lattice to be probed. We couple the probe site to an injection site of the lattice via a weak Bragg link, having an energy scale $t_{\rm inj}$, as shown in Fig. 1c. The probe site has a controllable energy bias relative to the lattice system, $E_{\rm inj}$, which is introduced via a detuning of the probe-system Bragg transition, $|0\rangle \leftrightarrow |1\rangle$. The lattice system under study is composed by coupling (via Bragg transitions) the momentum orders $p = 2n\hbar k$, where $n \geq 1$ and is truncated at a final value depending on the size of the lattice under study. In the described experiments, the lattices we consider involve no variations of their potential landscape, and are thus formed by resonantly coupling all of the relevant momentum orders. In the AAHH model[46,47,58] considered in simulations, detunings of the Bragg transitions are used to introduce quasiperiodic variations in the site energies.

In our experiments, all atoms initially start in the $p = 0$ order. The $p = 0$ order corresponds to the probe site in all of our lattice realizations. For one experimental run, we fix $E_{\rm inj}$ and let the atoms evolve under the influence of our engineered Hamiltonian for a variable duration τ. We then extract the population of the $p = 0$ state versus the evolution time τ, and fit this to an exponential, $N(0)e^{-\tau/\tau_0}$, where $N(0)$ is the initial atom number in the $p = 0$ order, which is the probe site. An examplar trace is shown in Fig. 1d. We repeat the experiment for many different $E_{\rm inj}$, and in the end we plot τ_0, the loss time, as a function of $E_{\rm inj}$, shown in Fig. 1e. When $E_{\rm inj}$ is close in energy to an eigenstate of the lattice, there will be a decrease in τ_0. This reflects the strong enhancement of the transition rate from the probe site when $E_{\rm inj}$ is in the vicinity of a lattice eigenenergy, due to the technique's sensitivity to the system density of states.

The ideal tight binding Hamiltonian (Eq. (3)) does not account for off-resonant Bragg transitions and the inhomogeneous (in real-space) many-body interactions in the momentum state lattice. These introduce on-site energy shifts[22,38,59] and consequently affect our experimental observations. To fully account for the aforementioned effects, we perform 3D mean-field Gross–Pitaevskii equation (GPE) simulations taking into account the experimentally measured atom number, trap frequencies, and hopping amplitudes (Bragg field strengths). The details on how to resolve the momentum space dynamics with the time evolution of spatial GPE are described in Ref. [60]. The loss time constant τ_0 is calculated from the dynamics of the number of atoms remaining in the original condensate momentum order ($p = 0$), normalized to the initial atom number. While the integration of the GPE under a time-dependent Bragg field can help to address the effects from mean-field interactions and the external dipole trap, the decoherence caused by long-time thermal fluctuations (e.g., inelastic collisions between different momentum states and momentum broadening due to finite temperature) and quantum depletion beyond the mean-field approximation are beyond the scope of our mean-field simulations.

References

1. Gaebler, J. P. et al. Observation of pseudogap behaviour in a strongly interacting fermi gas. *Nat. Phys.* **6**, 569 (2010).
2. Cheuk, L. W. et al. Spin-injection spectroscopy of a spin-orbit coupled fermi gas. *Phys. Rev. Lett.* **109**, 095302 (2012).
3. Wang, P. et al. Spin-orbit coupled degenerate fermi gases. *Phys. Rev. Lett.* **109**, 095301 (2012).
4. Greiner, M., Mandel, O., Esslinger, T., Hänsch, T. W. & Bloch, I. Quantum phase transition from a superfluid to a mott insulator in a gas of ultracold atoms. *Nature* **415**, 39 (2002).
5. Stöferle, T., Moritz, H., Schori, C., Köhl, M. & Esslinger, T. Transition from a strongly interacting 1d superfluid to a mott insulator. *Phys. Rev. Lett.* **92**, 130403 (2004).
6. Rajagopal, S. V. et al. Phasonic spectroscopy of a quantum gas in a quasicrystalline lattice. *Phys. Rev. Lett.* **123**, 223201 (2019).
7. Ernst, P. T. et al. Probing superfluids in optical lattices by momentum-resolved bragg spectroscopy. *Nat. Phys.* **6**, 56 (2010).
8. Fläschner, N. et al. High-precision multiband spectroscopy of ultracold fermions in a nonseparable optical lattice. *Phys. Rev. A* **97**, 051601 (2018).
9. Valdés-Curiel, A., Trypogeorgos, D., Marshall, E. E. & Spielman, I. B. Fourier transform spectroscopy of a spin–orbit coupled bose gas. *N. J. Phys.* **19**, 033025 (2017).
10. Sanchez-Palencia, L. & Lewenstein, M. Disordered quantum gases under control. *Nat. Phys.* **6**, 87 (2010).
11. Cooper, N. R., Dalibard, J. & Spielman, I. B. Topological bands for ultracold atoms. *Rev. Mod. Phys.* **91**, 015005 (2019).
12. Semeghini, G. et al. Measurement of the mobility edge for 3d anderson localization. *Nat. Phys.* **11**, 554 (2015).
13. Lüschen, H. P. et al. Single-particle mobility edge in a one-dimensional quasiperiodic optical lattice. *Phys. Rev. Lett.* **120**, 160404 (2018).
14. An, F. A. et al. Interactions and mobility edges: Observing the generalized aubry-andré model. *Phys. Rev. Lett.* **126**, 040603 (2021).
15. Ganeshan, S., Pixley, J. H. & Das Sarma, S. Nearest neighbor tight binding models with an exact mobility edge in one dimension. *Phys. Rev. Lett.* **114**, 146601 (2015).
16. Ozawa, T. & Price, H. M. Topological quantum matter in synthetic dimensions. *Nat. Rev. Phys.* **1**, 349 (2019).
17. Stuhl, B. K., Lu, H.-I., Aycock, L. M., Genkina, D. & Spielman, I. B. Visualizing edge states with an atomic bose gas in the quantum hall regime. *Science* **349**, 1514 (2015).
18. Mancini, M. et al. Observation of chiral edge states with neutral fermions in synthetic hall ribbons. *Science* **349**, 1510 (2015).

19. Chalopin, T. et al. Probing chiral edge dynamics and bulk topology of a synthetic hall system. *Nat. Phys.* **16**, 1017 (2020).
20. Roell, R. V., Laskar, A. W., Huybrechts, F. R. & Weitz, M. Chiral edge dynamics and quantum hall physics in synthetic dimensions with an atomic erbium bose-einstein condensate. *Phys. Rev. A* **107**, 043302 (2023).
21. Li, H. et al. Aharonov-bohm caging and inverse anderson transition in ultracold atoms. *Phys. Rev. Lett.* **129**, 220403 (2022).
22. Gou, W. et al. Tunable nonreciprocal quantum transport through a dissipative aharonov-bohm ring in ultracold atoms. *Phys. Rev. Lett.* **124**, 070402 (2020).
23. Wang, Y. et al. Observation of interaction-induced mobility edge in an atomic aubry-andré wire. *Phys. Rev. Lett.* **129**, 103401 (2022).
24. Wang, D.-W., Liu, R.-B., Zhu, S.-Y. & Scully, M. O. Superradiance lattice. *Phys. Rev. Lett.* **114**, 043602 (2015).
25. Wang, D.-W., Cai, H., Yuan, L., Zhu, S.-Y. & Liu, R.-B. Topological phase transitions in superradiance lattices. *Optica* **2**, 712 (2015).
26. Cai, H. et al. Experimental observation of momentum-space chiral edge currents in room-temperature atoms. *Phys. Rev. Lett.* **122**, 023601 (2019).
27. He, Y. et al. Flat-band localization in creutz superradiance lattices. *Phys. Rev. Lett.* **126**, 103601 (2021).
28. Mao, R. et al. Measuring zak phase in room-temperature atoms. *Light.: Sci. Appl.* **11**, 291 (2022).
29. Xu, X. et al. Floquet superradiance lattices in thermal atoms. *Phys. Rev. Lett.* **129**, 273603 (2022).
30. Lapp, S., Ang'ong'a, J., An, F. A. & Gadway, B. Engineering tunable local loss in a synthetic lattice of momentum states. *N. J. Phys.* **21**, 045006 (2019).
31. Kanungo, S. K. et al. Realizing topological edge states with rydberg-atom synthetic dimensions. *Nat. Commun.* **13**, 972 (2022).
32. Liang, Q. et al. Dynamic signatures of non-hermitian skin effect and topology in ultracold atoms. *Phys. Rev. Lett.* **129**, 070401 (2022).
33. Yang, D., Laflamme, C., Vasilyev, D. V., Baranov, M. A. & Zoller, P. Theory of a quantum scanning microscope for cold atoms. *Phys. Rev. Lett.* **120**, 133601 (2018).
34. Kollath, C., Köhl, M. & Giamarchi, T. Scanning tunneling microscopy for ultracold atoms. *Phys. Rev. A* **76**, 063602 (2007).
35. Gruss, D., Chien, C.-C., Barreiro, J. T., Ventra, M. D. & Zwolak, M. An energy-resolved atomic scanning probe. *N. J. Phys.* **20**, 115005 (2018).
36. Goldman, N. et al. Direct imaging of topological edge states in cold-atom systems. *Proc. Natl Acad. Sci.* **110**, 6736 (2013).
37. An, F. A., Meier, E. J. & Gadway, B. Engineering a flux-dependent mobility edge in disordered zigzag chains. *Phys. Rev. X* **8**, 031045 (2018).
38. An, F. A., Meier, E. J., Ang'ong'a, J. & Gadway, B. Correlated dynamics in a synthetic lattice of momentum states. *Phys. Rev. Lett.* **120**, 040407 (2018).
39. Gaunt, A. L., Schmidutz, T. F., Gotlibovych, I., Smith, R. P. & Hadzibabic, Z. Bose-einstein condensation of atoms in a uniform potential. *Phys. Rev. Lett.* **110**, 200406 (2013).
40. Tajik, M. et al. Designing arbitrary one-dimensional potentials on an atom chip. *Opt. Express* **27**, 33474 (2019).
41. D'Errico, C. et al. Feshbach resonances in ultracold ^{39}K. *N. J. Phys.* **9**, 223 (2007).
42. Chapurin, R. et al. Precision test of the limits to universality in few-body physics. *Phys. Rev. Lett.* **123**, 233402 (2019).
43. Etrych, Jcv et al. Pinpointing feshbach resonances and testing efimov universalities in ^{39}K. *Phys. Rev. Res.* **5**, 013174 (2023).
44. Aidelsburger, M. et al. Realization of the hofstadter hamiltonian with ultracold atoms in optical lattices. *Phys. Rev. Lett.* **111**, 185301 (2013).
45. Miyake, H., Siviloglou, G. A., Kennedy, C. J., Burton, W. C. & Ketterle, W. Realizing the harper hamiltonian with laser-assisted tunneling in optical lattices. *Phys. Rev. Lett.* **111**, 185302 (2013).
46. Harper, P. G. Single band motion of conduction electrons in a uniform magnetic field. *Proc. Phys. Soc. Sect. A* **68**, 874 (1955).
47. Hofstadter, D. R. Energy levels and wave functions of bloch electrons in rational and irrational magnetic fields. *Phys. Rev. B* **14**, 2239 (1976).
48. Roati, G. et al. Anderson localization of a non-interacting bose–einstein condensate. *Nature* **453**, 895 (2008).
49. Das, K. K. & Christ, J. Realizing the harper model with ultracold atoms in a ring lattice. *Phys. Rev. A* **99**, 013604 (2019).
50. Lau, A., Ortix, C. & van den Brink, J. Topological edge states with zero hall conductivity in a dimerized hofstadter model. *Phys. Rev. Lett.* **115**, 216805 (2015).
51. Aidelsburger, M. et al. Measuring the chern number of hofstadter bands with ultracold bosonic atoms. *Nat. Phys.* **11**, 162 (2015).
52. Ni, X. et al. Observation of hofstadter butterfly and topological edge states in reconfigurable quasi-periodic acoustic crystals. *Commun. Phys.* **2**, 55 (2019).
53. Ye, F. & Sun, X. Hofstadter butterfly and topological edge states in a quasiperiodic photonic crystal cavity array. *Opt. Express* **30**, 26620 (2022).
54. Binnig, G. & Rohrer, H. Scanning tunneling microscopy—from birth to adolescence. *Rev. Mod. Phys.* **59**, 615 (1987).
55. Agrawal, S., Paladugu, S. N. M. & Gadway, B. Two dimensional momentum state lattices. Preprint at *arXiv* https://doi.org/10.48550/arXiv.2305.17987 (2023).
56. Gadway, B. Atom-optics approach to studying transport phenomena. *Phys. Rev. A* **92**, 043606 (2015).
57. Meier, E. J., An, F. A. & Gadway, B. Atom-optics simulator of lattice transport phenomena. *Phys. Rev. A* **93**, 051602 (2016).
58. Aubry, S. & André, G. Analyticity breaking and anderson localization in incommensurate lattices. *Ann. Isr. Phys. Soc.* **3**, 18 (1980).
59. An, F. A. et al. Nonlinear dynamics in a synthetic momentum-state lattice. *Phys. Rev. Lett.* **127**, 130401 (2021).
60. Chen, T., Xie, D., Gadway, B. & Yan, B. A gross-pitaevskii-equation description of the momentum-state lattice: roles of the trap and many-body interactions. Preprint at *arXiv* https://doi.org/10.48550/arXiv.2103.14205 (2021).

Author contributions

F.A.A. and S.N.M.P. collected the experimental data. T.C. wrote and performed the numerical GPE simulations. F.A.A. and S.N.M.P. performed additional numerical simulations of idealized tight-binding models. S.N.M.P., with the assistance of B.G., wrote the paper. All authors contributed to the project planning and development. B.G. and B.Y. supervised the project.

Competing interests

The authors declare no competing interests.

Additional information

Correspondence and requests for materials should be addressed to Bryce Gadway.

Peer review information *Communications Physics* thanks the anonymous reviewers for their contribution to the peer review of this work.

Reprints and permission information is available at http://www.nature.com/reprints

Publisher's note Springer Nature remains neutral with regard to jurisdictional claims in published maps and institutional affiliations.